PHYSICS

Entangling free electrons and optical excitations

Andrea Konečná[1,2], Fadil Iyikanat[1], F. Javier García de Abajo[1,3]*

The inelastic interaction between flying particles and optical nanocavities gives rise to entangled states in which some excitations of the latter are paired with momentum changes in the former. Specifically, free-electron entanglement with nanocavity modes opens appealing opportunities associated with the strong interaction capabilities of the electrons. However, the achievable degree of entanglement is currently limited by the lack of control over the resulting state mixtures. Here, we propose a scheme to generate pure entanglement between designated optical-cavity excitations and separable free-electron states. We shape the electron wave function profile to select the accessible cavity modes and simultaneously associate them with targeted electron scattering directions. This concept is exemplified through theoretical calculations of free-electron entanglement with degenerate and nondegenerate plasmon modes in silver nanoparticles and atomic vibrations in an inorganic molecule. The generated entanglement can be further propagated through its electron component to extend quantum interactions beyond existing protocols.

INTRODUCTION

Although entangled states in the context of quantum optics are generally relying on photons (1, 2), the exploration of entanglement with other types of information carriers could open a wealth of possibilities to find previously unexplored phenomena and materialize disruptive protocols for quantum metrology and microscopy (3–5). In particular, free electrons are advantageous candidates because they can undergo substantial inelastic scattering by nanostructures (6), which is an attribute enabling electron energy-loss spectroscopy (EELS) performed in electron microscopes to reveal the presence, strength, and spatial distribution of optical excitations down to the atomic scale (7–13). Actually, low-loss EELS has been extensively used to study atomic vibrations in low-dimensional materials (14, 15) and molecules (16–19), collective excitations such as plasmons (20–24) and phonon polaritons (11, 25–27), and photon confinement in optical cavities (28–30).

In momentum-resolved EELS, each excitation event produced by a traversing electron is individually identified through an electron measurement as a function of the deflection angle and energy loss (31–33), and therefore, this configuration already generates entanglement between electron states with different energy/momentum and excitations in the sampled structure. Consequently, the post-interaction electron-sample state has the form

$$| \Psi_f \rangle = \sum_n \int d^2 \mathbf{Q}_f \, \alpha^f_{\mathbf{Q}_f n} | \mathbf{Q}_f \rangle \otimes | n \rangle \qquad (1)$$

where n and $\mathbf{Q}_f$ run over final sample and electron-wave-vector states, respectively, and $\alpha^f_{\mathbf{Q}_f n}$ are complex scattering amplitudes (13). In some simple scenarios, such as the interaction with translationally invariant structures supporting surface polaritons, the excitation of these modes is associated with the transfer of definite amounts of energy and momentum, thus producing electron entanglement with a continuum of optical modes, which reveals their dispersion relation when measuring the electrons as a function of energy loss and deflection angle (31, 33–36). Entangled states produced by interaction

with a polaritonic band in a translationally invariant specimen can even include the creation of multiple surfaces modes (32, 37, 38), as reported in the first experimental evidence of surface plasmons (37). However, for localized modes and, generally, in the interaction with photonic cavities, the resulting electron-specimen mixture of states is too complex to be of practical interest for quantum technologies.

Free-electron waves can be manipulated with great precision thanks to an impressive series of advances that occurred in electron microscopy over the past decades. Now, electron beams (e-beams) can be collimated and focused with sub-ångstrom spatial precision (39), as well as monochromatized and energy-filtered within a few millielectronvolt energy resolution (11, 25). In addition to traditional electron-optics elements such as lenses (40) and beam splitters (41–43), electron waves can be laterally shaped into on-demand profiles through static (44, 45) and programmable (46) plates, as well as through interaction with spatially modulated optical fields (47–51). The manipulation of the longitudinal electron wave function component is also possible in ultrafast electron microscopes (52), which enable temporal electron-pulse compression down to attosecond (53–55) time scales, and further endows free electrons with the ability to transfer quantum coherence among different systems (56, 57). The field is thus ripe for the exploitation of free electrons as additional elements in the quantum technology Lego, but as impressive as these advances may seem, they have not yet been leveraged to generate pure entanglement between light and free electrons in which only a few quantum states are involved in Eq. 1.

Here, we demonstrate through rigorous quantum theory that pure entanglement between electrons and confined optical modes can be generated by suitably patterning the transverse incident electron wave function. As schematically illustrated in Fig. 1A, the electron undergoes a change in the direction of propagation after being inelastically scattered by a specimen, and we prepare the incident electron wave profile (amplitude and phase) in such a way that only a few sample excitations are accessible (two in the figure), leading to separable transmission directions (transverse wave vectors $\mathbf{Q}_1$ and $\mathbf{Q}_2$). The two possible excitations created by the electron together with their different associated scattering directions form an entangled state. In essence, we specify a finite volume in the configuration space of transmitted electrons defined by an energy-loss window $\Delta \hbar \omega$ and a transverse momentum area $\Delta \hbar \mathbf{Q}_f$ in which the final state only

[1]ICFO-Institut de Ciencies Fotoniques, The Barcelona Institute of Science and Technology, Castelldefels, Barcelona 08860, Spain. [2]Central European Institute of Technology, Brno University of Technology, Brno 61200, Czech Republic. [3]ICREA-Institució Catalana de Recerca i Estudis Avançats, Passeig Lluís Companys 23, 08010 Barcelona, Spain.
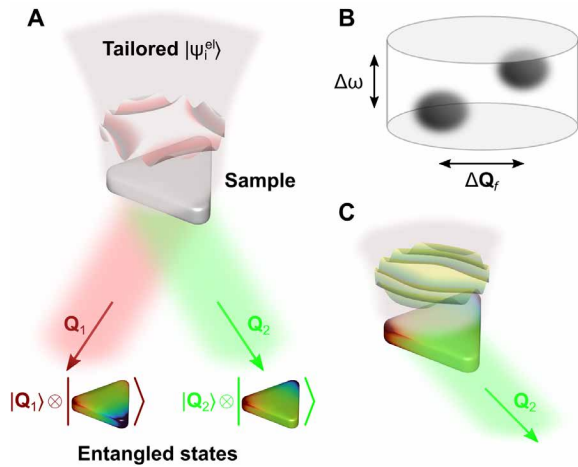*Corresponding author. Email: javier.garciadeabajo@nanophotonics.es

Fig. 1. Proposed scheme for the generation of entangled electron–cavity states.
(**A**) A preshaped electron interacts with a nanostructure (a triangular plasmonic cavity) supporting well-defined optical or vibrational modes. The incident electron wave function $|\psi_i^{el}\rangle$ is tailored such that we obtain entangled states after interaction, correlating different specimen excitations (colored triangles) with separated electron scattering directions (final electron state having components of transverse wave vectors $\mathbf{Q}_1$ and $\mathbf{Q}_2$). A maximally entangled electron-specimen state is thus produced as the sample is in a superposition of excited states correlated with different electron scattering directions. (**B**) Electrons are emerging along separate spots within a finite region of size $\Delta\hbar\omega \times \Delta\hbar\mathbf{Q}_f$ in the configuration space of energy-loss and transverse-momentum transfers. (**C**) Momentum filtering at the electron detector allows us to project on the desired sample mode and eventually explore its dynamics through subsequent interrogation, for example, by exposure to a synchronized light pulse.

populates two well-defined spots (Fig. 1B). As we demonstrate below, this approach can also be used to create heralded single sample excitations (Fig. 1C). In addition, manipulation of the electron component in electron–sample entangled states through, for example, electron interference could be used to process quantum information and imprint it on other (eventually macroscopic) objects via subsequent interactions.

RESULTS

Free-electron interaction with confined optical modes

We intend to synthesize an electron–sample state, as described by Eq. 1, with the free-electron component piled up at separate regions in momentum–energy space (Fig. 1B) and a different sample excitation associated with each of those regions. The starting point is the initial combined state

$$|\Psi_i\rangle = |\psi_i^{el}\rangle \otimes |0\rangle$$

where the specimen is in its ground state $|0\rangle$ and the incident electron wave function, whose spatial dependence is given by

$$\psi_i^{el}(\mathbf{R}) = \int d^2\mathbf{Q}_i\, \alpha_{\mathbf{Q}_i}^i (e^{i\mathbf{Q}_i\cdot\mathbf{R}}/2\pi) \tag{2}$$

is prepared as a combination of momentum states with coefficients $\alpha_{\mathbf{Q}_i}^i$ determined through the use of customized transmission masks (44, 45, 58) or phase imprinting based on electrostatic (46) and optical (47, 49) fields. We consider incident monochromatic electrons,

such that the dependence of the electron wave function on two-dimensional (2D) transverse coordinates $\mathbf{R}$ and its decomposition in 2D wave vectors $\mathbf{Q}_i$ is everything we need to describe the electron in the interaction region without loss of generality.

The electron–specimen interaction operates a linear transformation relating the final coefficients $\alpha_{\mathbf{Q}_f,n}^f$ in Eq. 1 to $\alpha_{\mathbf{Q}_i}^i$ in Eq. 2. More precisely,

$$\alpha_{\mathbf{Q}_f,n}^f = \int d^2\mathbf{Q}_i\, M_{\mathbf{Q}_f-\mathbf{Q}_i,n}\, \alpha_{\mathbf{Q}_i}^i \tag{3}$$

where $M_{\mathbf{Q}_f-\mathbf{Q}_i,n}$ only depends on the momentum transfer $\hbar(\mathbf{Q}_i - \mathbf{Q}_f)$ for each excited state n (see Methods).

A connection can be readily established to EELS experiments, in which electron counts are recorded as a function of the energy loss $\hbar\omega$, thus yielding a frequency- and momentum-resolved loss probability $\Gamma_{EELS}(\mathbf{Q}_f, \omega) = \sum_n |\alpha_{\mathbf{Q}_f,n}^f|^2 \delta(\omega - \omega_n)$, where $\hbar\omega_n$ is the excitation energy of the sample mode n. Within first-order perturbation theory and further adopting the electrostatic and nonrecoil approximations, the angle-resolved EELS probability can be expressed in terms of mode-dependent dimensionless spectral functions $g_n(\omega)$ as

$$\Gamma_{EELS}(\mathbf{Q}_f, \omega) = \frac{e^2}{4\pi^3\hbar v^2} \sum_n g_n(\omega)$$
$$\times \left| \int d^2\mathbf{R}\, \psi_i^{el}(\mathbf{R})\, e^{-i\mathbf{Q}_f\cdot\mathbf{R}}\, w_n(\mathbf{R}, \omega) \right|^2 \tag{4}$$

where v is the electron velocity and

$$w_n(\mathbf{R}, \omega) \propto \int d^2\mathbf{Q}\, e^{i\mathbf{Q}\cdot\mathbf{R}}\, M_{\mathbf{Q},n} \tag{5}$$

describes the spatial profile of mode n [see details in Methods, including expressions for the quantities $g_n(\omega)$ and $w_n(\mathbf{R}, \omega)$ associated with plasmons and atomic vibrations].

Here, we are interested in determining the incident electron wave function profile (i.e., the momentum-dependent coefficients $\alpha_{\mathbf{Q}_i}^i$) such that different sample modes n are associated with final wave function coefficients $\alpha_{\mathbf{Q}_f,n}^f$ within well-separated regions in momentum space (see Fig. 1B). To demonstrate the feasibility of this concept in the synthesis of electron–sample entanglement, we invert Eq. 3 with a predetermined choice of $\alpha_{\mathbf{Q}_f,n}^f$, which we set to designated values for each sample excitation n within a targeted finite-size region in $\mathbf{Q}_f$ space (see details in Methods). This simple procedure is sufficient for the proof-of-principle demonstration that we pursue in this work. However, in one of the examples, we present further improvement of the results when using an iterative method. Other schemes for incident electron wave function optimization could rely on neural-network training (59).

Selected excitation of individual plasmons

As a preliminary step before addressing electron–sample entanglement, we tackle the problem of selectively exciting a single plasmon in a metallic nanoparticle. Although this can be achieved through post-selection of a small range of scattered electron wave vectors (42), we formulate a solution in which the plasmon-exciting electrons emerge within a relatively large region in momentum space, and this solution is generalized below to create entanglement. We consider a silver triangle that sustains five plasmon modes in the spectral region between 2.4 and 3.7-eV spectral region (60): two sets of doubly degenerate dipolar (blue curve and circles, $n = 1,2$) and quadrupolar (red, $n = 4,5$) plasmons

and one nondegenerate hexapolar mode (green, $n = 3$), as revealed by the spatial and spectral functions plotted in Fig. 2 (A and B) (see details of the calculation in Methods). We then optimize the incident electron wave function over a finite $\mathbf{Q}_i$ region discretized with 1257 pixels and defined by a convergence half-angle $\varphi_i = 1.5$ mrad, such that either $n = 1,2$ or $n = 3$ is the only mode excited when the scattered electrons are collected over a $\mathbf{Q}_f$ region spanning a half-angle $\varphi_f = 0.75$ mrad (discretized with 49 pixels) and energy-filtered between 2.4 and 3.3 eV. Incidentally, modes $n = 1$ and 2 are dipolar, so they can be effectively excited in the aloof configuration, while mode $n = 3$ is hexapolar and requires the electron to pass closer to the particle to be excited.

The resulting real-space profiles of $\psi_i^{\mathrm{el}}(\mathbf{R})$ are shown in the insets of Fig. 2C (circular color plots; see also fig. S6A for the incident electron wave functions in $\mathbf{Q}_i$ space), along with the color-matched EELS probability curves obtained from Eq. 4 by collecting only electrons that emerge within the indicated $\mathbf{Q}_f$ and energy region. In a typical experimental scenario 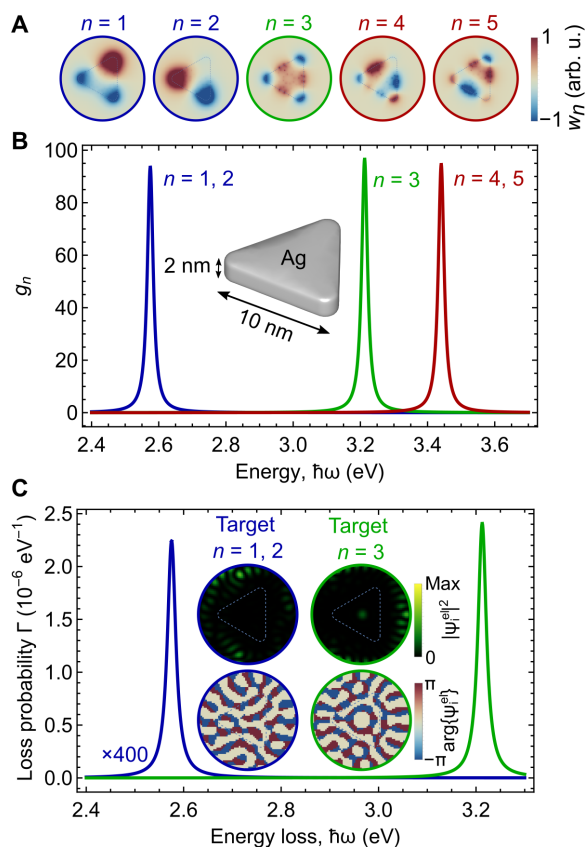with an unshaped electron beam, multiple modes are excited by the incident electron because they have overlapping spatial distributions (Fig. 2A), and the EELS probability integrated over all possible $\mathbf{Q}_f$'s is rigorously given by the incoherent average over incident electron positions $\mathbf{R}$, weighted by the electron probability $|\psi_i^{\mathrm{el}}(\mathbf{R})|^2$ (see Methods) (6, 61). However, our simple optimization procedure is capable of placing the weight of the excitation of either $n = 1,2$ or $n = 3$ mode preferably inside the $\mathbf{Q}_f$ region defined by a collection half-angle $\varphi_f = 0.75$ mrad. Such an optimization can be performed for smaller or larger convergence and collection angles as shown in fig. S1.

Generation of electron–plasmon entangled states

We now apply the principle of ψ_i^{el} shaping to demonstrate the generation of electron–sample entanglement for the same triangular particle as considered above. Specifically, we focus on the lowest-energy degenerate plasmons $n = 1,2$ (i.e., we consider post-selection of these final states by an energy filter) and aim at correlating these excitations with final electron momentum states along separate $\mathbf{Q}_f$ directions (Fig. 3A). By maximizing the fraction of the signal associated with the targeted excitation in each respective $\mathbf{Q}_f$ direction through the steepest-descent method, we find the optimized electron wave function shown in real space in Fig. 3B (and in momentum space in fig. S6B), from which we obtain the actual scattered electron distribution plotted in Fig. 3C in $\mathbf{Q}_f$ space for components corresponding to the excitation of $n = 1$ (top) and $n = 2$ (bottom) modes.

When examining the resulting degree of entanglement, we express the final electron–sample state after energy filtering and momentum post-selection by two apertures defined by the orange circles in Fig. 3C as

$$
\begin{aligned}
|\Psi_f\rangle =\ & (p_{11}|\mathbf{Q}_1\rangle + p_{12}|\mathbf{Q}_2\rangle) \otimes |1\rangle \\
& + (p_{22}|\mathbf{Q}_2\rangle + p_{21}|\mathbf{Q}_1\rangle) \otimes |2\rangle
\end{aligned}
\tag{6}
$$

where we assume that the apertures are small enough so that each of them captures coherently scattered electrons characterized by a well-defined state $|\mathbf{Q}_f\rangle$ with $f = 1,2$ (in practice, each of them can be a coherent superposition of plane waves transmitted through the finite solid angle region spanned by each aperture). To achieve pure entanglement, we require $p_{nm} \to 0$ for $n \neq m$ terms in Eq. 6, which happens after the noted numerical optimization: We obtain values $p_{11}^2/(p_{11}^2 + p_{21}^2) = 0.999991$ and $p_{22}^2/(p_{22}^2 + p_{12}^2) = 0.999779$, confirming a high degree of entanglement (62). Incidentally, a more direct inversion procedure without optimization still yields a level of entanglement exceeding 90% (fig. S2).

We note that the symmetry of the selected degenerate plasmons plays a similar role as photon polarization in light-based entanglement schemes (1). In the present instance, the electron wave function profiles are strongly affected by the threefold symmetry of the plasmonic nanoparticles and the choice of correlated electron output angles. Optimized profiles for more symmetric nanoparticles also become more symmetric, as shown for silver disks in fig. S3, where a high degree of entanglement (>99% mode separation) is achieved by direct inversion.

Electron entanglement with atomic vibrational states

The electron–sample entanglement scheme under consideration can be applied to sample excitations of different nature. We illustrate this versatility by considering atomic vibrations in a hexagonal boron
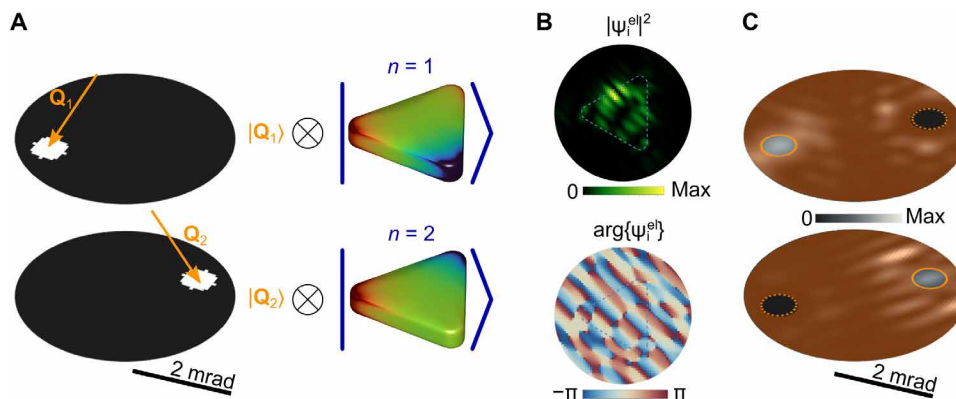

Fig. 2. Selective excitation of plasmon modes in a silver nanotriangle. (**A** and **B**) Spatial profiles (A) and spectral functions (B) associated with plasmons in a silver nanotriangle with a thickness of 2 nm and a side length of 10 nm. We find two sets of degenerate modes (blue and red peaks) and one nondegenerate mode (green; see color labels matched with the index n). (**C**) Electron energy-loss spectra for two optimized incident electron wave function profiles $\psi_i^{\mathrm{el}}(\mathbf{R})$. The insets show maps of the probability density and phase of the incident wave functions in the space of transverse coordinates $\mathbf{R}$, framed in color-matched circumferences. The optimization is carried out for 100 keV electrons, an electron detector consisting of 49 pixels, an incident convergence half-angle $\varphi_i = 1.5$ mrad, and a collection half-angle $\varphi_f = 0.75$ mrad. The nanotriangle contour is indicated by thin dashed lines in (A) and (C).

Fig. 3. Creation of electron–sample states with a high degree of entanglement. (**A**) Pursued electron–sample entangled state, consisting of the superposition of selected (by means of two apertures) electron momentum states within the white pixels in $\mathbf{Q}_f$ space (left) and correlated degenerate dipolar plasmons in the silver nanotriangle sample considered in Fig. 2 (right). (**B**) Spatial profile of the optimized incident wave function $\psi_i^{el}(\mathbf{R})$ required to produce the final state in (A). The contour of the triangular nanoparticle is indicated with dashed lines. (**C**) Resulting probability distributions $|\langle \mathbf{Q}_f, n | \Psi_f \rangle|^2$ with $n = 1$ (top) and $n = 2$ (bottom) in $\mathbf{Q}_f$ space, where each aperture (small circles) transmits nearly 100% of the targeted excitation n. The area outside the apertures (intended to be masked) is colored to emphasize the selected momentum regions of interest. The optimization is carried out for 100 keV electrons, 81 pixels in each of the detector apertures, $\varphi_i = 4$ mrad, and $\varphi_f = 2$ mrad.

nitride (hBN) molecule (Fig. 4), which we simulate from first principles (see Methods) (*63*) assuming passivation of the edges with hydrogen atoms. This structure supports a number of vibrational excitations up to energies ~450 meV, including a set of triply degenerate N—H bond-stretching modes at 440 meV (see EELS spectrum in fig. S4), on which we focus our analysis. We again optimize the incident electron wave function to achieve entanglement between final electron states and vibrational modes of the molecule [see the resulting $\psi_i^{el}(\mathbf{R})$ and $\psi_i^{el}(\mathbf{Q}_i)$ profiles in figs. S5 and S6C]. Because of the strong spatial confinement of vibrational modes, the angular ranges that need to be used for the incident and scattered electron wave functions are now considerably larger than for plasmons (cf. angle scales in Figs. 3 and 4). The achieved electron–sample state, illustrated in Fig. 4B, exhibits a decent degree of entanglement when selecting electrons scattered along the colored circles in $\mathbf{Q}_f$ space, also revealed through the partial probabilities contributed by each of the three vibrational modes to each of the regions enclosed by those circles (see table in Fig. 4C).

DISCUSSION

By entangling the transverse momenta of free electrons with localized optical excitations in a nanostructure, we could selectively measure one of the corresponding outgoing electron directions, thus providing a way to herald the creation of single designated excitations in the studied specimen. This should allow us to follow the dynamics of the latter and gain insight into the state-dependent decay pathways, for example, by subsequently probing the evolution of the specimen through scattering of laser pulses that are synchronized with the electron in an electron-pump/photon-probe approach. An additional possibility is offered by correlating the angle-resolved electron signal with traces originating in the decay of excited states of the specimen (e.g., an electrical signal produced by coupling to electron-hole pairs in a proximal semiconductor or also the polarization- and angle-resolved cathodoluminescence emission associated with radiative decay). The present scheme could further be extended to incorporate gain processes similar to those in photon-induced near-

field electron microscopy (PINEM) (*54*) upon illumination of the sample with symmetry-matched optical pulses that can simultaneously excite a subset of its supported excitations.

We remark that the proposed approach holds elements of novelty with respect to traditional quantum optics methods because one of the entangled particles (the free electron) can be highly energetic and, therefore, capable of undergoing subsequent strong collisions with other objects. These collisions could, for instance, trigger chemical reactions that would then be entangled with optical modes in the specimen with which the electron has previously interacted.

Although we have illustrated some possibilities based on heuristic electron wave function designs and a straightforward application of the steepest-descent maximization method, improved solutions to the problem of entanglement optimization could be obtained through neural-network training (*59*), possibly combined with iterative physical improvement of the wave function profile based on currently explored tunable electron phase plates (*46–51*). As an alternative to the use of aloof interaction with the optical modes of the sampled nanostructure to avoid strong electron collisions with atomic potentials, this type of adaptive improvement could potentially be used to compensate for the effect of these potentials and morphological imperfections. In addition to the investigated examples of plasmons in nanoparticles and atomic vibrations in molecules, we envision the entanglement of free electrons with optical modes in dielectric cavities (*30*) and photons guided along optical waveguides (*64*), which together configure a vast range of possibilities for leveraging the quantum nature of free electrons in the design of improved microscopy and metrology schemes.

METHODS

Transfer matrix for inelastic electron–sample scattering

The time-dependent electron–sample system can be generally described by a wave function of the form $|\psi(t)\rangle = \sum_n \int d^3\mathbf{q}\, \alpha_{\mathbf{q},n}(t)\, e^{-i(\epsilon_\mathbf{q}+\omega_n)t} |\mathbf{q}\rangle \otimes |n\rangle$, where $|\mathbf{q}\rangle$ and $|n\rangle$ are electron and sample eigenstates of the noninteracting Hamiltonian with energies $\hbar\epsilon_q$ and $\hbar\omega_n$, respectively. In particular, electron states are labeled by the 3D
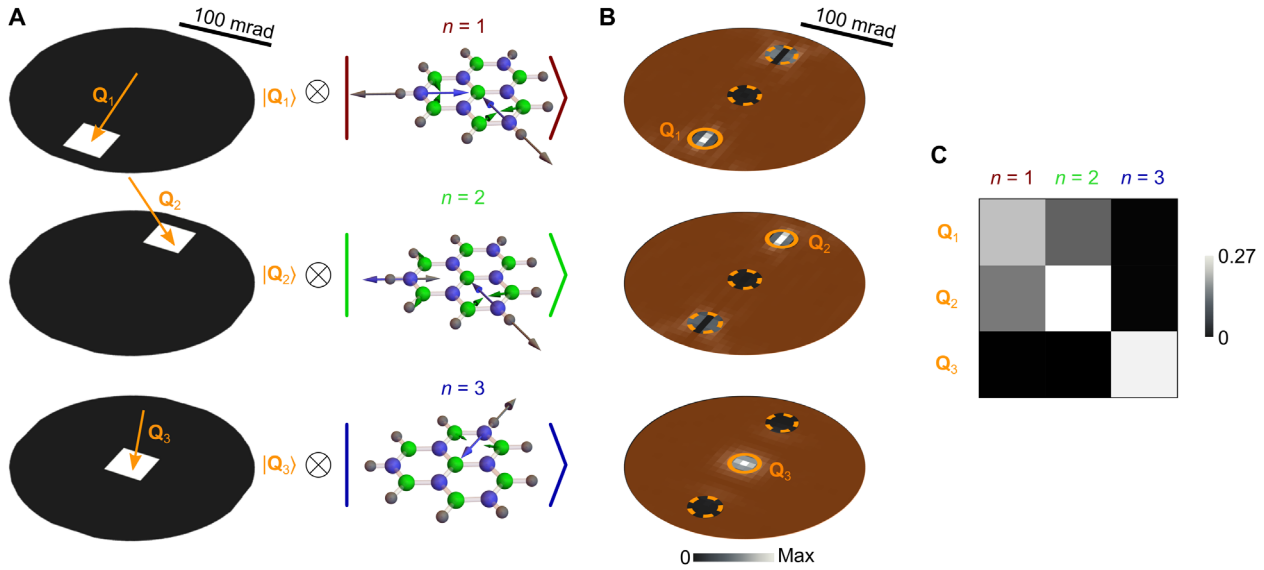
Fig. 4. Entanglement of free electrons and atomic vibrations. (**A**) Pursued electron–sample entangled state, consisting of the superposition of selected (by means of three apertures) electron-momentum states within the white pixels in $\mathbf{Q}_f$ space (left) and correlated triply degenerate 440-meV vibrational modes of an hBN molecule (right). (**B**) Resulting probability distributions $|\langle \mathbf{Q}_f, n | \Psi_f \rangle|^2$ with $n = 1$ (top), $n = 2$ (middle), and $n = 3$ (bottom) in $\mathbf{Q}_f$ space. The area outside the apertures (small circles) is colored to emphasize the selected momentum regions of interest. (**C**) Probability matrix showing the fractional contribution associated with the excitation of each of the three vibrational modes $n = 1$ to 3 to the energy-filtered electron signal contained within the three selected circular areas around final transverse wave vectors $\mathbf{Q}_1$, $\mathbf{Q}_2$, and $\mathbf{Q}_3$ in (A). The sum of the nine matrix elements is normalized to one. We consider 60 keV electrons, 29 detector pixels, and $\varphi_i = \varphi_f = 100$ mrad.

momentum $\hbar\mathbf{q}$ and satisfy the orthonormality relation $\langle \mathbf{q} | \mathbf{q}' \rangle = \delta(\mathbf{q} - \mathbf{q}')$. The expansion coefficients $\alpha_{\mathbf{q},n}(t)$ are determined by solving the Schrödinger equation with an electron–sample interaction Hamiltonian $\hat{\mathcal{H}}_1$, which is generally weak for the energetic electrons that are typically used in electron microscopes, so we can work within first-order perturbation theory. Then, taking the sample to be initially prepared in its ground state $n = 0$, the post-interaction wave function has coefficients $\alpha_{\mathbf{q},n}(\infty) = (-2\pi i/\hbar) \int d^3\mathbf{q}'\, \delta(\epsilon_{\mathbf{q}} - \epsilon_{\mathbf{q}'} + \omega_n) \langle n | \langle \mathbf{q} | \hat{\mathcal{H}}_1 | \mathbf{q}' \rangle | 0 \rangle \alpha_{\mathbf{q}',0}(-\infty)$, where we set $\omega_0 = 0$ without loss of generality. We further adopt the nonrecoil approximation (*13*) $\epsilon_{\mathbf{q}} - \epsilon_{\mathbf{q}'} \approx (\mathbf{q} - \mathbf{q}') \cdot \mathbf{v}$ under the assumption that the transverse electron energy is negligible compared with the longitudinal energy along the e-beam direction defined by the average electron velocity $\mathbf{v}$. This condition is commonly satisfied in electron microscopes. In this approximation, the energy $\hbar\omega_n$ transferred from the electron to the sample is fully absorbed by a change in the longitudinal electron wave vector given by $-\omega_n/v$, so for monochromatic incident electrons, the initial and final longitudinal components of the electron wave function play a trivial role and can be disregarded in the description of the present problem. Consequently, we can expand the final wave function as shown in Eq. 1, with coefficients $\alpha^f_{\mathbf{Q}_f n} \equiv \alpha_{\mathbf{q},n}(\infty)$ that only depend on the transverse electron wave vector $\mathbf{Q}_f$ for each sample excitation n and are determined from the incident electron wave function coefficients $\alpha^i_{\mathbf{Q}_i} \equiv \alpha_{\mathbf{q},0}(-\infty)$ through the linear relation $\alpha^f_{\mathbf{Q}_f n} = \int d^2\mathbf{Q}_i\, M_{\mathbf{Q}_f-\mathbf{Q}_i, n} \alpha^i_{\mathbf{Q}_i}$ (Eq. 3) with

$$M_{\mathbf{Q}_f-\mathbf{Q}_i, n} = \frac{-2\pi i}{\hbar v} \langle n | \langle \mathbf{q}_f | \hat{\mathcal{H}}_1 | \mathbf{q}_i \rangle | 0 \rangle \tag{7}$$

We remark that the transfer matrix elements defined in Eq. 7 involve just the difference between incident and scattered transverse wave vectors. In what follows, we develop a formalism to relate $M_{\mathbf{Q}_f-\mathbf{Q}_i n}$

to the EELS probability and obtain specific expressions for plasmonic and atomic-vibration modes.

EELS with shaped electron beams

We consider the configuration of Fig. 1A and assume the electron velocity and sample dimensions to be small enough as to neglect retardation effects and work in the electrostatic regime. Further adopting the aforementioned nonrecoil approximation, we can disregard the longitudinal component of the electron wave function and only consider the dependence on transverse coordinates $\mathbf{R} = (x, y)$ (i.e., taking the electron velocity $\mathbf{v}$ along z). We can then write a general expression for the EELS probability $\Gamma_{\text{EELS}}(\omega)$ in terms of the energy loss $\hbar\omega$, the transverse wave vector $\mathbf{Q}_f \perp \hat{z}$ of the final (f) electron state (corresponding to a wave function $\propto e^{i\mathbf{Q}_f \cdot \mathbf{R}}$), and the transverse component of the initial (i) electron wave function, $\psi_i(\mathbf{R})$. More precisely, using equation 17 of (*6*), we have $\Gamma_{\text{EELS}}(\omega) = \int d^2\mathbf{Q}_f \Gamma_{\text{EELS}}(\mathbf{Q}_f, \omega)$, where

$$\Gamma_{\text{EELS}}(\mathbf{Q}_f, \omega) = \frac{e^2}{4\pi^3 \hbar v^2} \int d^2\mathbf{R} \int d^2\mathbf{R}'\, \psi_i(\mathbf{R}) \psi_i^*(\mathbf{R}')$$
$$\times e^{i\mathbf{Q}_f \cdot (\mathbf{R}'-\mathbf{R})} \mathcal{W}(\mathbf{R}, \mathbf{R}', \omega) \tag{8}$$

is the momentum-resolved probability and

$$\mathcal{W}(\mathbf{R}, \mathbf{R}', \omega) = \int_{-\infty}^{\infty} dz \int_{-\infty}^{\infty} dz'\, e^{i\omega(z-z')/v} \times \text{Im}\{-W(\mathbf{r}, \mathbf{r}', \omega)\} \tag{9}$$

is a transverse screened interaction obtained from the full screened interaction $W(\mathbf{r}, \mathbf{r}', \omega)$. The latter stands for the Coulomb potential created at $\mathbf{r}$ by a point charge of magnitude $e^{-i\omega t}$ placed at $\mathbf{r}'$, including the effect of screening by the environment. Now, as we show below for plasmonic and phononic structures, the transverse screened interaction in Eq. 9 is separable as

$$\mathcal{W}(\mathbf{R}, \mathbf{R}', \omega) = \sum_n g_n(\omega)\, w_n(\mathbf{R}, \omega)\, w_n^*(\mathbf{R}', \omega) \tag{10}$$

where n runs over excitation modes characterized by spatial profiles $w_n(\mathbf{R}, \omega)$ and dimensionless spectral functions $g_n(\omega)$. Finally, inserting Eq. 10 into Eq. 8, we readily find Eq. 4 in the main text. Incidentally, the angle-integrated inelastic electron signal (i.e., the integral of Eq. 8 over $\mathbf{Q}_f$) reduces to $\Gamma_{\text{EELS}}(\omega) = (e^2/\pi\hbar v^2)\Sigma_n g_n(\omega)$ $\int d^2\mathbf{R} \, | \, \psi_i(\mathbf{R}) \, |^2 \, | \, w_n(\mathbf{R}, \omega) \, |^2$, which is an average over transverse positions $\mathbf{R}$ weighted by both the incident electron probability (6, 61) and the mode spatial profile, and consequently, because the e-beam can generally excite different modes n, the optimization scheme that we pursue here to produce entanglement essentially consists in rearranging the $\mathbf{Q}_f$ distribution of the scattered electron components associated with the excitation of each of those modes.

We note that the spectral functions in this formalism can be generally approximated by Lorentzians

$$g_n(\omega) \approx \text{Im}\left\{ \frac{G_n/\pi}{\omega_n - \omega - i\gamma_n/2} \right\}$$

peaked at the mode energies $\hbar\omega_n$ and having areas G_n and widths γ_n (see below) that determine the spectral positions and strengths of the EELS features.

Numerical determination of $|\psi_i^{\text{el}}\rangle$ for creating selected excitations and entangled electron–sample states

Given a desired final state defined through the coefficients $\alpha_{\mathbf{Q}_f,n}^f$, we numerically obtain $\alpha_{\mathbf{Q}_i}^i$ by inverting Eq. 3 upon discretization of $\mathbf{Q}_i$ using a finite number of points and pixels at the electron analyzer in the Fourier plane $\mathbf{Q}_f$, as noted in the main text. More precisely, we follow a simple procedure consisting in specifying target values of $\alpha_{\mathbf{Q}_f,n}^f$ within a region $Q < Q_{f,\text{max}}$ (effectively setting it to zero outside it) and obtain $\alpha_{\mathbf{Q}_i}^i$ for $Q_i < Q_{i,\,\text{max}}$ through the aforementioned numerical inversion method. The wave vector ranges are related to the maximum incidence|collection half-angle $\varphi_{i|f}$ through $Q_{i|f,\,\text{max}} = (m_e v/\hbar)$ $\sin \varphi_{i|f}$. In this scheme, to select a single sample excitation $n = n_0$ (Fig. 2), we set $\alpha_{\mathbf{Q}_f,n}^f = C\delta_{nn_0}\Theta(Q_{f,\text{max}} - Q_f)$, where C is a constant and Θ is the step function. However, to produce electron–sample entanglement involving two (Fig. 3) or three (Fig. 4) sample states n_j correlated with final electron wave vectors $\mathbf{Q}_j$ (see Fig. 1B), we set $\alpha_{\mathbf{Q}_f,n_j}^f$ to a constant at the $\mathbf{Q}_f$ space pixel that contains $\mathbf{Q}_j$ and zero elsewhere. We then construct $|\psi_i^{\text{el}}\rangle$ from the obtained coefficients $\alpha_{\mathbf{Q}_i}^i$ (also setting them to zero for $Q_i > Q_{i,\text{max}}$) and insert this input wave function in Eq. 4 to generate the actual final probability distributions, plotted in the figures with a finer discretization in $\mathbf{Q}_f$ space.

Transfer matrix from the spectral and spatial mode functions
An expression for the EELS probability analogous to Eq. 4 can be readily obtained from Eq. 3 as

$$\Gamma_{\text{EELS}}(\mathbf{Q}_f, \omega) = \sum_n \left| \int d^2\mathbf{Q}_i \, M_{\mathbf{Q}_f-\mathbf{Q}_i,n} \, \alpha_{\mathbf{Q}_i}^i \right|^2 \delta(\omega - \omega_n) \quad (11)$$

The connection between Eqs. 4 and 11 is established by adding finite mode widths γ_n to the latter and expanding the incident electron wave function in the former as an integral over momentum components, as indicated in Eq. 2. Comparing the two resulting expressions, we find

$$M_{\mathbf{Q},n} = \frac{e}{4\pi^2 v}\sqrt{\frac{G_n}{\pi\hbar}} \int d^2\mathbf{R} \, e^{-i\mathbf{Q}\cdot\mathbf{R}} \, w_n(\mathbf{R}, \omega) \quad (12)$$

which provides a prescription to obtain the transfer matrix coefficients defined in Eq. 7 directly from the screened interaction, thus bypassing the need for a detailed specification of the interaction Hamiltonian. Then, the spatial profiles in Eq. 5 are simply given by the inverse Fourier transform of Eq. 12.

Transfer matrix and transverse screened interaction for plasmonic nanoparticles
In the electrostatic limit under consideration, we can recast the response of an arbitrarily shaped homogeneous nanoparticle into an eigenvalue problem (65, 66). We then need to find the real eigenvalues λ_n and eigenvectors $\sigma_n(\mathbf{s})$ of the integral equation $2\pi\lambda_n\sigma_n(\mathbf{s}) = \oint d\mathbf{s}' F(\mathbf{s}, \mathbf{s}')\sigma_n(\mathbf{s}')$, where $\mathbf{s}$ and $\mathbf{s}'$ run over particle surface coordinates, $F(\mathbf{s}, \mathbf{s}') = -\hat{\mathbf{n}} \cdot (\mathbf{s} - \mathbf{s}')/| \, \mathbf{s} - \mathbf{s}' \, |^3$, and $\hat{\mathbf{n}}$ is the outer surface normal. Here, we solve this eigensystem for triangular particles using the MNPBEM toolbox (67) based on a finite boundary element discretization of the particle surface. Then, the spectral functions in Eq. 10 reduce to (65, 66)

$$g_n(\omega) = \text{Im}\left\{ \frac{-2}{\epsilon(1 + \lambda_n) + (1 - \lambda_n)} \right\}$$

whereas the spatial profiles become

$$w_n(\mathbf{R}, \omega) = 2\oint d\mathbf{s} \, \sigma_n(\mathbf{s}) \, e^{-i\omega s_z/v} K_0\left(\frac{\omega | \, \mathbf{R} - \mathbf{S} \, |}{v} \right)$$

with $\mathbf{s} = \mathbf{S} + s_z\hat{\mathbf{z}}$. This expression neglects the contribution of bulk modes, which should be a reasonable approximation at loss energies well below the bulk plasmon. Inserting it into Eq. 12, the transfer matrix elements reduce to

$$M_{\mathbf{Q},n} \approx \frac{e}{\pi v}\sqrt{\frac{G_n}{\pi\hbar}} \frac{1}{Q^2 + \omega_n^2/v^2} \oint d\mathbf{s} \, \sigma_n(\mathbf{s}) e^{-i(\mathbf{Q}+\hat{\mathbf{z}}\omega_n/v)\cdot\mathbf{s}}$$

where we have approximated $\omega \approx \omega_n$. For silver, we model the dielectric function as (6) $\epsilon = \epsilon_b - \omega_p^2/\omega(\omega + i\gamma)$ with $\epsilon_b = 4.0$, $\hbar\omega_p = 9.17$ eV, and $\hbar\gamma = 21$ meV, yielding mode frequencies $\omega_n = \omega_p/\sqrt{\epsilon_b + (1 - \lambda_n)/(1 + \lambda_n)}$, flat widths $\gamma_n \approx \gamma$, and spectral weights $G_n = \pi\omega_n^3/[\omega_p^2(1 + \lambda_n)]$.

Transfer matrix and transverse screened interaction for atomic vibrations
For molecules or nanoparticles whose mid-infrared response is dominated by atomic vibrations, we find the spectral and spatial dependence of the modes in Eq. 10 to be governed by (63, 68).

$$g_n(\omega) = \text{Im}\left\{ \frac{\omega_n^2}{\omega_n^2 - \omega(\omega + i\gamma)} \right\} \quad (13)$$

and

$$w_n(\mathbf{R}, \omega) = \frac{2}{\omega_n}\sum_l \frac{1}{\sqrt{M_l}} \int d^3\mathbf{r}' K_0(\omega | \, \mathbf{R} - \mathbf{R}' \, |/v) \, e^{i\omega z'/v} [\mathbf{e}_{nl} \cdot \vec{\rho}_l(\mathbf{r}')]$$

where n now runs over vibrational modes, ω_n and $\mathbf{e}_{nl}$ are the corresponding real frequencies and normalized atomic displacement vectors ($\Sigma_l \mathbf{e}_{nl} \cdot \mathbf{e}_{n'l} = \delta_{nn'}$), respectively, the l sum extends over the atoms in the structure, M_l is the mass of atom l, $\vec{\rho}_l(\mathbf{r})$ denotes the gradient of the charge distribution associated with displacements of that atom, and we have incorporated a phenomenological damping rate γ (here set to $\hbar\gamma = 1$ meV). From Eq. 13, we have $\gamma_n \approx \gamma$ for all modes and $G_n \approx \pi\omega_n/2$. Following (63), we use density functional

theory (DFT) to calculate $\vec{\rho}_l(\mathbf{r})$, ω_n, and e_{nl} (see below). The prescription $|\mathbf{R} - \mathbf{R}'| \rightarrow \sqrt{|\mathbf{R} - \mathbf{R}'|^2 + \Delta^2}$ is also adopted with $\Delta = 0.2$ Å to approximately account for a cutoff $\sim \hbar/\Delta$ in momentum transfer (6) and so avoid the unphysical divergence associated with close electron-atom encounters.

First-principles description of atomic vibrations

We use DFT and the projector augmented wave method (69) as implemented in the Vienna Ab initio Simulation Package (70–72) with the Perdew-Burke-Ernzerhof–generalized gradient approximation for electron exchange and correlation (73). This method is applied to describe hBN flakes with hydrogen-passivated edges using a plane wave cutoff energy of 500 eV and a sufficient amount of vacuum spacing in all directions around the structure to avoid interaction among the periodic images. Atomic equilibrium positions are found by minimizing the total energy using the conjugate gradient method with convergence criteria between consecutive iteration steps set to 10^{-5} eV for the total energy and 0.02 eV/Å for the atomic forces. Vibrational frequencies and eigenmodes are found by diagonalizing the dynamical matrix, which is calculated for 0.01-Å displacements. The corresponding gradients $\vec{\rho}_l(\mathbf{r})$ of the charge distribution are obtained by treating core electrons and nuclei as point particles, while the contribution coming from valence electrons is directly taken from DFT using a dense grid.

SUPPLEMENTARY MATERIALS

Supplementary material for this article is available at https://science.org/doi/10.1126/sciadv.abo7853

REFERENCES AND NOTES

1. R. Horodecki, P. Horodecki, M. Horodecki, K. Horodecki, Quantum entanglement. *Rev. Mod. Phys.* **81**, 865–942 (2009).
2. E. Togan, Y. Chu, A. S. Trifonov, L. Jiang, J. Maze, L. Childress, M. V. G. Dutt, A. S. Sörensen, P. R. Hemmer, A. S. Zibrov, M. D. Lukin, Quantum entanglement between an optical photon and a solid-state spin qubit. *Nature* **466**, 730–734 (2010).
3. O. Kfir, Entanglements of electrons and cavity photons in the strong-coupling regime. *Phys. Rev. Lett.* **123**, 103602 (2019).
4. V. Di Giulio, M. Kociak, F. J. García de Abajo, Probing quantum optical excitations with fast electrons. *Optica* **6**, 1524–1534 (2019).
5. O. Reinhardt, C. Mechel, M. Lynch, I. Kaminer, Free-electron qubits. *Ann. Phys.* **533**, 2000254 (2021).
6. F. J. García de Abajo, Optical excitations in electron microscopy. *Rev. Mod. Phys.* **82**, 209–275 (2010).
7. R. F. Egerton, *Electron Energy-Loss Spectroscopy in the Electron Microscope* (Plenum Press, 1996).
8. R. F. Egerton, New techniques in electron energy-loss spectroscopy and eneorgy-filtered imaging. *Micron* **34**, 127–139 (2003).
9. R. Erni, N. D. Browning, Valence electron energy-loss spectroscopy in monochromated scanning transmission electron microscopy. *Ultramicroscopy* **104**, 176–192 (2005).
10. R. Brydson, *Electron Energy Loss Spectroscopy* (BIOS Scientific Publishers, 2001).
11. O. L. Krivanek, T. C. Lovejoy, N. Dellby, T. Aoki, R. W. Carpenter, P. Rez, E. Soignard, J. Zhu, P. E. Batson, M. J. Lagos, R. F. Egerton, P. A. Crozier, Vibrational spectroscopy in the electron microscope. *Nature* **514**, 209–212 (2014).
12. O. L. Krivanek, N. Dellby, J. A. Hachtel, J.-C. Idrobo, M. T. Hotz, B. Plotkin-Swing, N. J. Bacon, A. L. Bleloch, G. J. Corbin, M. V. Hoffman, C. E. Meyer, T. C. Lovejoy, Progress in ultrahigh energy resolution EELS. *Ultramicroscopy* **203**, 60–67 (2019).
13. F. J. García de Abajo, V. Di Giulio, Optical excitations with electron beams: Challenges and opportunities. *ACS Photonics* **8**, 945–974 (2021).
14. F. S. Hage, G. Radtke, D. M. Kepaptsoglou, M. Lazzeri, Q. M. Ramasse, Single-atom vibrational spectroscopy in the scanning transmission electron microscope. *Science* **367**, 1124–1127 (2020).
15. X. Yan, C. Liu, C. A. Gadre, L. Gu, T. Aoki, T. C. Lovejoy, N. Dellby, O. L. Krivanek, D. G. Schlom, R. Wu, X. Pan, Single-defect phonons imaged by electron microscopy. *Nature* **589**, 65–69 (2021).
16. P. Rez, T. Aoki, K. March, D. Gur, O. L. Krivanek, N. Dellby, T. C. Lovejoy, S. G. Wolf, H. Cohen, Damage-free vibrational spectroscopy of biological materials in the electron microscope. *Nat. Commun.* **7**, 10945 (2016).
17. D. M. Haiber, P. A. Crozier, Nanoscale probing of local hydrogen heterogeneity in disordered carbon nitrides with vibrational electron energy-loss spectroscopy. *ACS Nano* **12**, 5463–5472 (2018).
18. J. R. Jokisaari, J. A. Hachtel, X. Hu, A. Mukherjee, C. Wang, A. Konečná, T. C. Lovejoy, N. Dellby, J. Aizpurua, O. L. Krivanek, J.-C. Idrobo, R. F. Klie, Vibrational spectroscopy of water with high spatial resolution. *Adv. Mater.* **12**, 430–436 (2018).
19. J. A. Hachtel, J. Huang, I. Popovs, S. Jansone-Popova, J. K. Keum, J. Jakowski, T. C. Lovejoy, N. Dellby, O. L. Krivanek, J. C. Idrobo, Identification of site-specific isotopic labels by vibrational spectroscopy in the electron microscope. *Science* **363**, 525–528 (2019).
20. M. Bosman, V. J. Keast, M. Watanabe, A. I. Maaroof, M. B. Cortie, Mapping surface plasmons at the nanometre scale with an electron beam. *Nanotechnology* **18**, 165505 (2007).
21. J. Nelayah, M. Kociak, O. Stéphan, F. J. García de Abajo, M. Tencé, L. Henrard, D. Taverna, I. Pastoriza-Santos, L. M. Liz-Marzán, C. Colliex, Mapping surface plasmons on a single metallic nanoparticle. *Nat. Phys.* **3**, 348–353 (2007).
22. D. Rossouw, G. A. Botton, Plasmonic response of bent silver nanowires for nanophotonic subwavelength waveguiding. *Phys. Rev. Lett.* **110**, 066801 (2013).
23. S. F. Tan, L. Wu, J. K. W. Yang, P. Bai, M. Bosman, C. A. Nijhuis, Quantum plasmon resonances controlled by molecular tunnel junctions. *Science* **343**, 1496–1499 (2014).
24. V. Mkhitaryan, K. March, E. Tseng, X. Li, L. Scarabelli, L. M. Liz-Marzán, S.-Y. Chen, L. H. G. Tizei, O. Stéphan, J.-M. Song, M. Kociak, F. J. García de Abajo, A. Gloter, Can copper nanostructures sustain high-quality plasmons? *Nano Lett.* **21**, 2444–2452 (2021).
25. M. J. Lagos, A. Trügler, U. Hohenester, P. E. Batson, Mapping vibrational surface and bulk modes in a single nanocube. *Nature* **543**, 529–532 (2017).
26. A. A. Govyadinov, A. Konečná, A. Chuvilin, S. Vélez, I. Dolado, A. Y. Nikitin, S. Lopatin, F. Casanova, L. E. Hueso, J. Aizpurua, R. Hillenbrand, Probing low-energy hyperbolic polaritons in van der Waals crystals with an electron microscope. *Nat. Commun.* **8**, 95 (2017).
27. N. Li, X. Guo, X. Yang, R. Qi, T. Qiao, Y. Li, R. Shi, Y. Li, K. Liu, Z. Xu, L. Liu, F. J. García de Abajo, Q. Dai, E.-G. Wang, P. Gao, Direct observation of highly confined phonon polaritons in suspended monolayer hexagonal boron nitride. *Nat. Mater.* **20**, 43–48 (2020).
28. O. Kfir, H. Lourenço-Martins, G. Storeck, M. Sivis, T. R. Harvey, T. J. Kippenberg, A. Feist, C. Ropers, Controlling free electrons with optical whispering-gallery modes. *Nature* **582**, 46–49 (2020).
29. K. Wang, R. Dahan, M. Shentcis, Y. Kauffmann, A. Ben Hayun, O. Reinhardt, S. Tsesses, I. Kaminer, Coherent interaction between free electrons and a photonic cavity. *Nature* **582**, 50–54 (2020).
30. Y. Auad, C. Hamon, M. Tencé, H. Lourenço-Martins, V. Mkhitaryan, O. Stéphan, F. J. García de Abajo, L. H. G. Tizei, M. Kociak, Unveiling the coupling of single metallic nanoparticles to whispering-gallery microcavities. *Nano Lett.* **22**, 319–327 (2022).
31. R. B. Pettit, J. Silcox, R. Vincent, Measurement of surface-plasmon dispersion in oxidized aluminum films. *Phys. Rev. B* **11**, 3116–3123 (1975).
32. O. L. Krivanek, Y. Tanishiro, K. Takayanagi, K. Yagi, Electron energy loss spectroscopy in glancing reflection from bulk crystals. *Ultramicroscopy* **11**, 215–222 (1983).
33. F. S. Hage, R. J. Nicholls, J. R. Yates, D. G. McCulloch, T. C. Lovejoy, N. Dellby, O. L. Krivanek, K. Refson, Q. M. Ramasse, Nanoscale momentum-resolved vibrational spectroscopy. *Sci. Adv.* **4**, eaar7495 (2018).
34. P. Shekhar, M. Malac, V. Gaind, N. Dalili, A. Meldrum, Z. Jacob, Momentum-resolved electron energy loss spectroscopy for mapping the photonic density of states. *ACS Photonics* **4**, 1009–1014 (2017).
35. C. Mechel, Y. Kurman, A. Karnieli, N. Rivera, A. Arie, I. Kaminer, Quantum correlations in electron microscopy. *Optica* **8**, 70–78 (2021).
36. Y. Adiv, H. Hu, S. Tsesses, R. Dahan, K. Wang, Y. Kurman, A. Gorlach, H. Chen, X. Lin, G. Bartal, I. Kaminer, Observation of 2D Cherenkov radiation, https://arxiv.org/abs/2203.01698 (2022).
37. C. J. Powell, J. B. Swan, Origin of the characteristic electron energy losses in aluminum. *Phys. Rev.* **115**, 869–875 (1959).
38. P. Schattschneider, F. Födermayr, D. S. Su, Coherent double-plasmon excitation in aluminum. *Phys. Rev. Lett.* **59**, 724–727 (1987).
39. P. E. Batson, N. Dellby, O. L. Krivanek, Sub-ångstrom resolution using aberration corrected electron optics. *Nature* **418**, 617–620 (2002).
40. L. Clark, A. Béché, G. Guzzinati, A. Lubk, M. Mazilu, R. Van Boxem, J. Verbeeck, Exploiting lens aberrations to create electron-vortex beams. *Phys. Rev. Lett.* **111**, 064801 (2013).
41. G. Möllenstedt, H. Düker, Beobachtungen und Messungen an Biprisma-Interferenzen mit Elektronenwellen. *Z. Phys.* **145**, 377–397 (1956).
42. G. Guzzinati, A. Beche, H. Lourenço-Martins, J. Martin, M. Kociak, J. Verbeeck, Probing the symmetry of the potential of localized surface plasmon resonances with phase-shaped electron beams. *Nat. Commun.* **8**, 14999 (2017).
43. C. W. Johnson, A. E. Turner, B. J. McMorran, Scanning two-grating free electron Mach-Zehnder interferometer. *Phys. Rev. Res.* **3**, 043009 (2021).

44. J. Verbeeck, H. Tian, P. Schattschneider, Production and application of electron vortex beams. *Nature* **467**, 301–304 (2010).

45. B. J. McMorran, A. Agrawal, I. M. Anderson, A. A. Herzing, H. J. Lezec, J. J. McClelland, J. Unguris, Electron vortex beams with high quanta of orbital angular momentum. *Science* **331**, 192–195 (2011).

46. J. Verbeeck, A. Béché, K. Müller-Caspary, G. Guzzinati, M. A. Luong, M. D. Hertog, Demonstration of a 2 × 2 programmable phase plate for electrons. *Ultramicroscopy* **190**, 58–65 (2018).

47. A. Konečná, F. J. García de Abajo, Electron beam aberration correction using optical near fields. *Phys. Rev. Lett.* **125**, 030801 (2020).

48. O. Schwartz, J. J. Axelrod, S. L. Campbell, C. Turnbaugh, R. M. Glaeser, H. Müller, Laser phase plate for transmission electron microscopy. *Nat. Methods* **16**, 1016–1020 (2019).

49. F. J. García de Abajo, A. Konečná, Optical modulation of electron beams in free space. *Phys. Rev. Lett.* **126**, 123901 (2021).

50. M. C. C. Mihaila, P. Weber, M. Schneller, L. Grandits, S. Nimmrichter, T. Juffmann, Transverse electron-beam shaping with light. *Phys. Rev. X* **12**, 031043 (2022).

51. I. Madan, V. Leccese, A. Mazur, F. Barantani, T. LaGrange, A. Sapozhnik, P. M. Tengdin, S. Gargiulo, E. Rotunno, J.-C. Olaya, I. Kaminer, V. Grillo, F. J. García de Abajo, F. Carbone, G. M. Vanacore, Ultrafast transverse modulation of free electrons by interaction with shaped optical fields. *ACS Photonics* **10**, 3215–3224 (2022).

52. S. A. Aseyev, E. A. Ryabov, B. N. Mironov, A. A. Ischenko, The development of ultrafast electron microscopy. *Crystals* **10**, 452 (2020).

53. P. Baum, A. H. Zewail, Attosecond electron pulses for 4D diffraction and microscopy. *Proc. Natl. Acad. Sci. U.S.A.* **104**, 18409–18414 (2007).

54. K. E. Priebe, C. Rathje, S. V. Yalunin, T. Hohage, A. Feist, S. Schäfer, C. Ropers, Attosecond electron pulse trains and quantum state reconstruction in ultrafast transmission electron microscopy. *Nat. Photonics* **11**, 793–797 (2017).

55. Y. Morimoto, P. Baum, Diffraction and microscopy with attosecond electron pulse trains. *Nat. Phys.* **14**, 252–256 (2018).

56. O. Kfir, V. Di Giulio, F. J. García de Abajo, C. Ropers, Optical coherence transfer mediated by free electrons. *Sci. Adv.* **7**, eabf6380 (2021).

57. V. Di Giulio, O. Kfir, C. Ropers, F. J. García de Abajo, Modulation of cathodoluminescence emission by interference with external light. *ACS Nano* **15**, 7290–7304 (2021).

58. M. Uchida, A. Tonomura, Generation of electron beams carrying orbital angular momentum. *Nature* **464**, 737–739 (2010).

59. S. R. Spurgeon, C. Ophus, L. Jones, A. Petford-Long, S. V. Kalinin, M. J. Olszta, R. E. Dunin-Borkowski, N. Salmon, K. Hattar, W.-C. D. Yang, R. Sharma, Y. Du, A. Chiaramonti, H. Zheng, E. C. Buck, L. Kovarik, R. L. Penn, D. Li, X. Zhang, M. Murayama, M. L. Taheri, Towards data-driven next-generation transmission electron microscopy. *Nat. Mater.* **20**, 274–279 (2021).

60. F. P. Schmidt, H. Ditlbacher, F. Hofer, J. R. Krenn, U. Hohenester, Morphing a plasmonic nanodisk into a nanotriangle. *Nano Lett.* **14**, 4810–4815 (2014).

61. R. H. Ritchie, A. Howie, Electron excitation and the optical potential in electron microscopy. *Philos. Mag.* **36**, 463–481 (1977).

62. A. F. Abouraddy, B. E. A. Saleh, A. V. Sergienko, M. C. Teich, Degree of entanglement for two qubits. *Phys. Rev. A* **64**, 050101 (2001).

63. A. Konečná, F. Iyikanat, F. J. García de Abajo, Theory of atomic-scale vibrational mapping and isotope identification with electron beams. *ACS Nano* **15**, 9890–9899 (2021).

64. X. M. Bendaña, A. Polman, F. J. García de Abajo, Single-photon generation by electron beams. *Nano Lett.* **11**, 5099–5103 (2011).

65. F. J. García de Abajo, J. Aizpurua, Numerical simulation of electron energy loss near inhomogeneous dielectrics. *Phys. Rev. B* **56**, 15873–15884 (1997).

66. G. Boudarham, M. Kociak, Modal decompositions of the local electromagnetic density of states and spatially resolved electron energy loss probability in terms of geometric modes. *Phys. Rev. B* **85**, 245447 (2012).

67. U. Hohenester, A. Trügler, MNPBEM - A matlab toolbox for the simulation of plasmonic nanoparticles. *Comput. Phys. Commun.* **183**, 370–381 (2012).

68. J. R. M. Saavedra, F. J. García de Abajo, Phonon excitation by electron beams in nanographenes. *Phys. Rev. B* **92**, 115449 (2015).

69. P. E. Blöchl, Projector augmented-wave method. *Phys. Rev. B* **50**, 17953–17979 (1994).

70. G. Kresse, J. Furthmüller, Efficient iterative schemes for ab initio total-energy calculations using a plane-wave basis set. *Phys. Rev. B* **54**, 11169–11186 (1996a).

71. G. Kresse, J. Hafner, *Ab initio* molecular dynamics for liquid metals. *Phys. Rev. B* **47**, 558–561 (1993).

72. G. Kresse, J. Furthmüller, Efficiency of ab-initio total energy calculations for metals and semiconductors using a plane-wave basis set. *Comput. Mater. Sci.* **6**, 15–50 (1996).

73. J. P. Perdew, K. Burke, M. Ernzerhof, Generalized gradient approximation made simple. *Phys. Rev. Lett.* **77**, 3865–3868 (1996).